8

ANALYSIS OF ANTENNAS WITH ELLIPTICAL APERTURES USING FOURIER-BESSEL EXPANSION: A COMPARATIVE STUDY

C. S. Kim and Y. Rahmat-Samii

8.1 Introduction

Future generation of satellite and ground antennas will require to radiate elliptical beams. One way to achieve an elliptical beam is to use reflector antennas with projected elliptical apertures. It is the purpose of this chapter to present a new mathematical/numerical method for the diffraction analysis of antennas with elliptical apertures.

For circular apertures, Jacobi-Bessel expansion methods [1,2] as well as Fourier-Bessel series techniques [3,4] are established and give very accurate numerical results. However, for elliptical apertures, the Fourier-Bessel technique has not been introduced yet even though the Jacobi-Bessel expansion method has been used already to produce several numerical results [5]. It is worthwhile to mention that the Jacobi-Bessel expansion is related to the well-known Zernike polynomials as presented in [6,7]. Although the Brute-Force FFT technique [8] is another possible method for elliptical apertures, it does not explicitly employ the elliptical geometry.

As shown by Rahmat-Samii in [5], the Jacobi-Bessel method works

very well for circular and low eccentricity elliptical apertures even if the aperture size is very large. However, for a high eccentricity elliptical aperture, the convergence behavior of the far field pattern is slowed and the computational efficiency is lowered. In this chapter, we develop the Fourier-Bessel expansion technique for elliptical apertures. The elliptical coordinate system is introduced and the radiation integral is expressed in terms of radial and angular Mathieu functions. Expression of the radiation integral in terms of radial and angular Mathieu functions is undesirable for machine computation, since it is a laborious task to evaluate the Mathieu functions. Direct use of this form of the radiation integral is less efficient than use of the Jacobi-Bessel method. However, the initial integrals can be simplified by use of the properties of the Mathieu functions and their relationships with the Bessel functions. The final integrals are written in terms of Bessel functions only. This result allows the Fourier-Bessel technique to be very efficient and useful, because, the Fast Fourier Transform (FFT) routines which are used to find coefficients of a Fourier series are very efficient nowadays and because we can calculate Bessel functions without the limitation of parameters.

The accuracy of the Fourier-Bessel algorithm is strongly dependent on the number of Fourier series terms. For a high eccentricity elliptical aperture, the Fourier-Bessel method is very efficient because it needs small number of series terms. However, for a large aperture, it requires many series terms which could result into long computing time.

Another purpose of this work is to compare the Jacobi-Bessel and Fourier-Bessel techniques and to find the convergence behaviors of both methods for various sizes and shapes of the elliptical aperture. The procedures discussed in this chapter are also applicable for any elliptically shaped aperture-type antennas with known aperture distributions.

8.2 Formulation of the Problem

For the theoretical analysis of the Fourier-Bessel technique, we start with the formula for the radiated far field pattern of a reflector with arbitrary projected aperture. That formula was reported in [2,4,5] and repeated below:

$$\overline{E} = -jk\eta(\hat{\hat{I}} - \hat{r}\hat{r}) \cdot \overline{T}(\theta, \phi) \frac{e^{-jkr}}{4\pi r} \tag{1}$$

where

$$\overline{T}(\theta,\phi) = \iint_S \overline{J}_s e^{jk\overline{\rho}\cdot\hat{r}}\, dS \tag{2}$$

$$\overline{\rho} = \hat{x}x + \hat{y}y + \hat{z}z \tag{3}$$

$$\hat{r} = \hat{x}\cos\phi\sin\theta + \hat{y}\sin\phi\sin\theta + \hat{z}\cos\theta \tag{4}$$

In the above expression, $\overline{T}(\theta,\phi)$ is the radiation integral, $\overline{J}_s$ is the induced current on the reflector surface (typically the physical optics current) and η is the free space impedance. To solve (2), the surface Jacobian transformation is introduced, i.e.,

$$\overline{T}(\theta,\phi) = \iint_A \overline{J}_s \sqrt{1 + \left(\frac{\partial z}{\partial x}\right)^2 + \left(\frac{\partial z}{\partial y}\right)^2}\, e^{ikz\cos\theta} \times e^{jk[(u-u_0)x+(v-v_0)y]}\, e^{jk(u_0x+v_0y)}\, dx\,dy \tag{5}$$

where $(u_0, v_0) = (\cos\phi_0 \sin\theta_0, \sin\phi_0 \sin\theta_0)$ is the anticipated main beam direction, $(u, v) = (\cos\phi \sin\theta, \sin\phi \sin\theta)$ is the space representation, $\hat{\hat{I}}$ is the identity dyadic and A is the projected area in the xy-plane.

The offset parabolic surface description can be written as

$$z = \frac{(x+H)^2 + y^2}{4F} - F \tag{6}$$

where F is the focal length of the paraboloid and H is the offset height parameter as is shown in Fig. 8.1. By substituting (5) and (6) into (2) and using the Taylor's series expansion, (5) can be expressed as

$$\overline{T}(\theta,\phi) = \sum_{p=0}^{\infty} \overline{T}_p(\theta,\phi) \tag{7}$$

where

$$\overline{T}_p(\theta,\phi) = \frac{1}{p!}\left(\frac{jk}{4F}\right)^p (\cos\theta - \cos\theta_0)^p e^{jk(\frac{H^2}{4F}-F)\cos\theta} \times \iint_A {}^p\overline{J}_{eq}\, e^{jk[(u-u_o+\frac{H}{2F}(\cos\theta-\cos\theta_0))x+(v-v_o)y]}\, dx\,dy \tag{8}$$

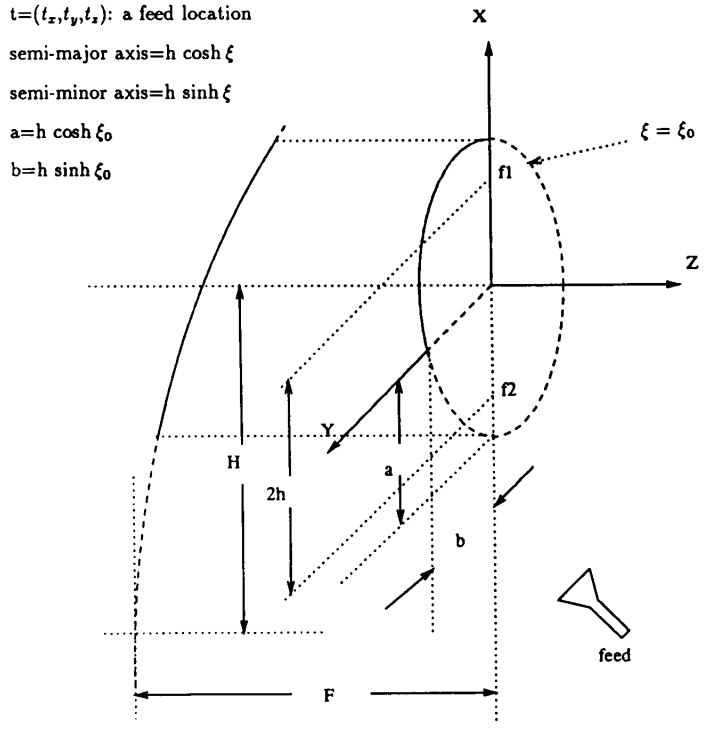

Figure 8.1 Geometry of an offset parabolic reflector antenna with an elliptical aperture. The projected aperture is located in the xy-plane and a feed is located at $t = (t_x, t_y, t_z)$. Both the rectangular and the elliptical coordinates systems are used.

and

$$ {}_p\overline{J}_{eq} = \overline{J}_s \sqrt{1 + \left(\frac{\partial z}{\partial x}\right)^2 + \left(\frac{\partial z}{\partial y}\right)^2}\, e^{\frac{jk}{4F}(x^2+y^2)\cos\theta_0} \times e^{ik\left[\left(u_0 + \frac{H}{2F}\cos\theta_0\right)x + v_0 y\right]} (x^2+y^2)^p \qquad (9) $$

Now, the truncation function R is defined as

$$ R = \begin{cases} 1, & \text{inside the area } A \\ 0, & \text{outside the area } A \end{cases} \qquad (10) $$

Then, ${}_p\overline{J}_{eq}$ can be expressed as

$$ {}_p\overline{J}_{eq} = R\,\overline{g} \tag{11} $$

where $\overline{g}$ is a vector function whose value is equal to ${}_p\overline{J}_{eq}$ inside the area A. And its value outside the area A is extrapolated from the value of ${}_p\overline{J}_{eq}$ inside the area A [4]. If $\overline{g}$ is expanded in a Fourier series in a rectangular area of $2a$ by $2b$ dimensions, we have

$$ {}_p\overline{J}_{eq} = R \sum_{m=-\infty}^{\infty} \sum_{n=-\infty}^{\infty} {}_p\overline{g}_{mn}\, e^{-j(\frac{m\pi}{a}x + \frac{n\pi}{b}y)} \tag{12} $$

where the Fourier coefficients ${}_p\overline{g}_{mn}$ are independent of (θ, ϕ).

Substituting (12) into (8) produces

$$ \overline{T}_p(\theta,\phi) = \frac{1}{p!}\left(\frac{jk}{4F}\right)^p (\cos\theta - \cos\theta_0)^p e^{jk(\frac{H^2}{4F} - F)\cos\theta} \times R \sum_{m=-\infty}^{\infty} \sum_{n=-\infty}^{\infty} {}_p\overline{g}_{mn}\, R_{mn} \tag{13} $$

where

$$ R_{mn} = \iint_A e^{jk[(u-u_o + \frac{H}{2F}(\cos\theta - \cos\theta_o) - \frac{m\pi}{ka})x + (v - v_o - \frac{n\pi}{kb})y]}\, dx\,dy \tag{14} $$

For the elliptical aperture shown in Fig. 8.1, we use the elliptical coordinate system [9]. First, parameters B_{mn} and Φ_{mn} are defined as follows:

$$ B_{mn} = \sqrt{\left(u - u_0 + \frac{H}{2F}(\cos\theta - \cos\theta_0) - \frac{m\pi}{ka}\right)^2 + \left(v - v_0 - \frac{n\pi}{kb}\right)^2} \tag{15} $$

$$ \Phi_{mn} = \tan^{-1}\left(\frac{v - v_0 - \frac{n\pi}{kb}}{u - u_0 + \frac{H}{2F}(\cos\theta - \cos\theta_0) - \frac{m\pi}{ka}}\right) \tag{16} $$

By substituting (15) and (16) into (14), R_{mn} can be expressed with the elliptical coordinate as follows [10]:

$$
\begin{aligned}
R_{mn} &= \int_0^{\xi_0}\int_0^{2\pi} e^{jkB_{mn}h[\cosh\xi\cos\eta\cos\Phi_{mn}+\sinh\xi\sin\eta\sin\Phi_{mn}]} \\
&\quad\times \frac{h^2}{2}(\cosh 2\xi - \cos 2\eta)d\xi d\eta \\
&= h^2\int_0^{\xi_0}\int_0^{2\pi}\sum_{r=0}^{\infty}\left[\frac{1}{p_{2r}}Ce_{2r}(\xi,q_{mn})ce_{2r}(\eta,q_{mn})ce_{2r}(\Phi_{mn},q_{mn})\right. \\
&\quad+\frac{j}{p_{2r+1}}Ce_{2r+1}(\xi,q_{mn})ce_{2r+1}(\eta,q_{mn})ce_{2r+1}(\Phi_{mn},q_{mn}) \\
&\quad+\frac{1}{s_{2r+2}}Se_{2r+2}(\xi,q_{mn})se_{2r+2}(\eta,q_{mn})se_{2r+2}(\Phi_{mn},q_{mn}) \\
&\quad\left.+\frac{j}{s_{2r+1}}Se_{2r+1}(\xi,q_{mn})se_{2r+1}(\eta,q_{mn})se_{2r+1}(\Phi_{mn},q_{mn})\right] \\
&\quad\times(\cosh 2\xi - \cos 2\eta)\,d\xi d\eta
\end{aligned}
\tag{17}
$$

where $Ce_r(\xi,q_{mn})$ is even radial Mathieu function, $Se_r(\xi,q_{mn})$ is odd radial Mathieu function, $ce_r(\eta,q_{mn})$ and $se_r(\eta q_{mn})$ are even and odd angular Mathieu functions respectively, p_r and s_r are joining factors which are defined in [10], h is the half distance between the foci of the ellipse and

$$q_{mn} = \frac{1}{4}k^2B_{mn}^2h^2 \tag{18}$$

The solution of (17) is derived in the Appendix A and is given below

$$R_{mn} = -\frac{4\pi}{k^2B_{mn}^2}\sum_{r=0}^{\infty}A_0^{(2r)}ce_{2r}(\Phi_{mn},q_{mn})Ce'_{2r}(\xi_0,q_{mn})/p_{2r} \tag{19}$$

where prime denotes differentiation with respect to ξ_0.

Now, if one uses the following mathematical relationships between Mathieu functions and Bessel functions [10],

$$\frac{Ce_{2r}(\xi_0,q_{mn})ce_{2r}(\Phi_{mn},q_{mn})}{p_{2r}} = \sum_{i=0}^{\infty}(-1)^iA_{2i}^{(2r)}\cos 2i\alpha J_{2i}(z) \tag{20}$$

where

$$z = kB_{mn}h\sqrt{\cosh^2\xi_0\cos^2\Phi_{mn}+\sinh^2\xi_0\sin^2\Phi_{mn}} \tag{21}$$

$$\alpha = \tan^{-1}\left(\frac{\sinh\xi_0\sin\Phi_{mn}}{\cosh\xi_0\cos\Phi_{mn}}\right) \tag{22}$$

and the orthogonality properties of angular Mathieu function [10]:

$$\sum_{r=0}^{\infty} A_0^{(2r)} A_{2i}^{(2r)} = \begin{cases} 1/2, & \text{if } i = 0 \\ 0, & \text{otherwise} \end{cases} \tag{23}$$

R_{mn} can be expressed very simply as follows:

$$R_{mn} = \frac{2\pi ab J_1\left(k\sqrt{u_{mn}^2 a^2 + v_{mn}^2 b^2}\right)}{k\sqrt{u_{mn}^2 a^2 + v_{mn}^2 b^2}} \tag{24}$$

where

$$u_{mn} = B_{mn} \cos \Phi_{mn} \tag{25}$$

$$v_{mn} = B_{mn} \sin \Phi_{mn} \tag{26}$$

As shown in (24), R_{mn} is now expressed in terms of Bessel functions, only. This is a generalization of expressions given in [3].

8.3 Numerical Analysis

In this section, we present several numerical results which compare the computational efficiencies of the Fourier-Bessel and the Jacobi-Bessel methods of performing the physical optics integrations. Here, the feed patterns are approximated by linearly polarized $\cos^q(\theta)$ type pattern [11]. The values of q_1 for elevation xz-plane and q_2 for azimuth yz-planes are adjusted to provide the desired aperture taper.

In the previous section, we expressed the final results with a triply infinite sum but we must truncate the infinite series to finite sums for numerical computation. For the Fourier-Bessel technique, the truncated form is

$$\overline{T}(\theta,\phi) = \sum_{p=0}^{P} \frac{1}{p!}\left(\frac{jk}{4F}\right)^p (\cos\theta - \cos\theta_0)^p e^{jk\left(\frac{H^2}{4F} - F\right)\cos\theta} \times R \sum_{m=-M/2}^{M/2-1} \sum_{n=-N/2}^{N/2-1} {}_p\bar{g}_{mn} R_{mn} \tag{27}$$

where P is any positive integer but M and N should be integral powers of 2 because the FFT subprogram is used to find coefficients

of a Fourier series. The FFT algorithm is well established and very efficient nowadays. For the Jacobi-Bessel technique, the formula was expressed in [5]. Here, we just modify that into the truncated form as follows:

$$\begin{aligned}\overline{T}(\theta,\phi) = 2\pi \sum_{p=0}^{P} ab\, e^{ikz_c(w-w_B)} \frac{1}{p!}(jk)^p (w-w_B)^p \sum_{m=0}^{M} \sum_{n=0}^{N} (j)^n \\ \times \left[{}_p\overline{C}_{mn} \cos n\Phi + {}_p\overline{D}_{mn} \sin n\Phi \right] \\ \times \sqrt{2(n+2m+1)}\, \frac{J_{n+2m+1}(kB)}{kB} \end{aligned} \tag{28}$$

where P, M and N are positive integers and

$$\begin{aligned} B &= \sqrt{a^2(u-u_0)^2 + b^2(v-v_0)} \\ \Phi &= \tan^{-1} \frac{b(v-v_0)}{a(u-u_0)} \\ z_c &= \frac{H^2}{4F} - F \\ w &= \cos\theta \\ w_B &= \cos\theta_0 \end{aligned} \tag{29}$$

Figures 8.2 and 8.3 show that the results from the Jacobi-Bessel and the Fourier-Bessel expansion techniques agree with each other for a circular aperture $(a/b = 1.0)$ and an elliptical aperture $(a/b = 2.0)$, respectively. Usually the Fourier-Bessel technique requires more series terms than Jacobi-Bessel does but the FFT subprogram used in the Fourier-Bessel program is much faster than the integration subprogram used in the Jacobi-Bessel method. Thus, their computing times are comparable. For example, to produce the plots in Fig. 8.3, the Fourier-Bessel algorithm $(P = 2, M = 16, N = 8)$ required 0.53 minutes execution while the Jacobi-Bessel algorithm $(P = 2, M = 16, N = 8)$ needed 0.67 minutes with an IBM 3090 in the UCLA Computer Center.

Figures 8.4 and 8.5 illustrate how each series term contributes to the radiated far field patterns. In Fig. 8.4, we can see the dominant term $(m = 0, n = 0)$ has maximum values at boresight but other terms also contribute to the gain at boresight even though their values are much smaller. However, Fig. 8.5 shows that the Jacobi-Bessel series behaves very differently. Patterns of dominant terms of both methods

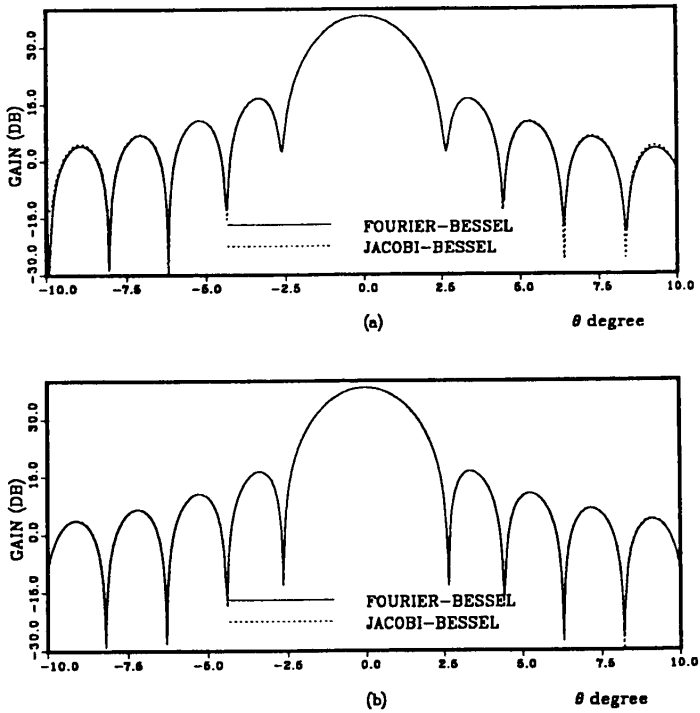

Figure 8.2 Comparative study between Fourier-Bessel and Jacobi-Bessel algorithm as applied to an offset parabolic antenna with a circular aperture, $a = 15\lambda$, $a/b = 1.0$, $F = 30\lambda$, $H = 18\lambda$, $q_1 = 7.14$, $q_2 = 7.14$, $t = (-18\lambda, 0, 0)$, $P, M, N = (1, 16, 16)$ and (1,7,7) for Fourier-Bessel and Jacobi-Bessel algorithm respectively; (a) $\phi = 0°$, (b) $\phi = 90°$.

are similar but patterns of other series terms are very different and only the dominant term $(m = 0, n = 0)$ of the Jacobi-Bessel expansion contributes at boresight.

For a large elliptical aperture $(a = 50\lambda)$, the Fourier-Bessel method requires large values of M and N but the Jacobi-Bessel method doesn't as is shown in Figs. 8.6 and 8.7. Also, the values of M and N for the Fourier-Bessel technique should be integer powers of 2 and those values are proportional to the area of the aperture. Thus, for a large and low eccentricity ellipse, Fourier-Bessel requires much longer computing time than does Jacobi-Bessel as is shown in Table 8.1. However, for a high eccentricity ellipse $(a/b = 5.0)$, Figs. 8.8 and 8.9 show that the Jacobi-Bessel has very slow convergence behavior

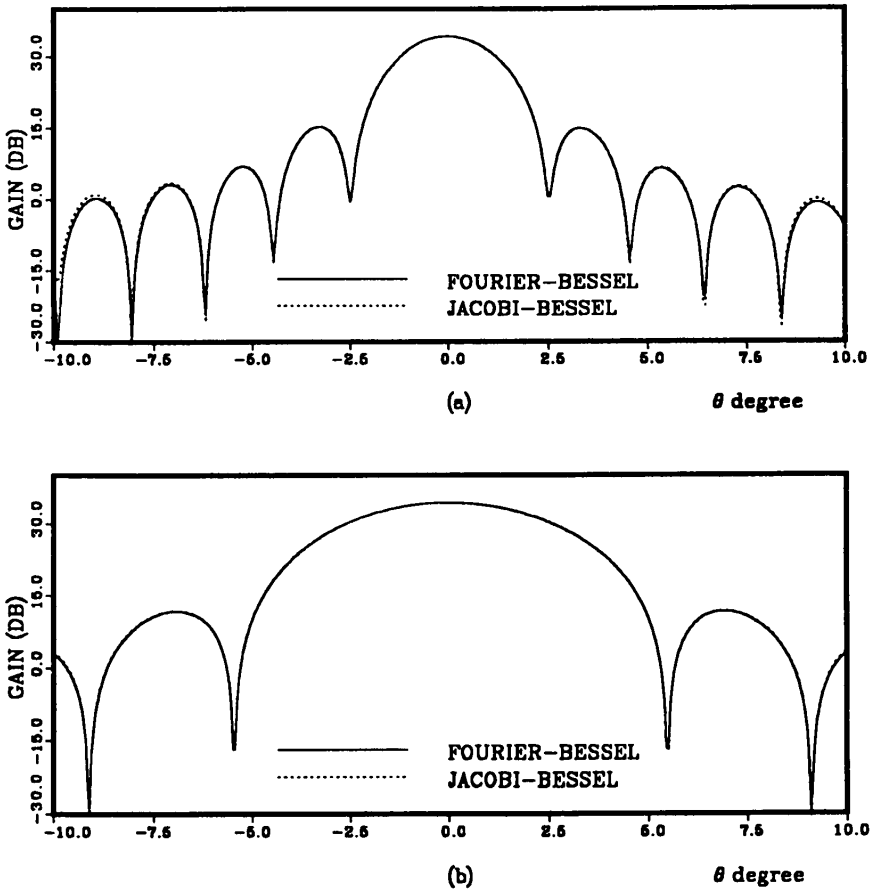

Figure 8.3 Comparative study between Fourier-Bessel and Jacobi-Bessel algorithm as applied to an offset parabolic antenna with an elliptical aperture, $a = 15\lambda$, $a/b = 2.0$, $F = 30\lambda$, $H = 18\lambda$, $q_1 = 7.14$, $q_2 = 44.9$, $t = (-18\lambda, 0, 0)$, $P, M, N = (1, 16, 8)$ and (1,7,7) for Fourier-Bessel and Jacobi-Bessel algorithm respectively; (a) $\phi = 0°$, (b) $\phi = 90°$.

and takes twice as long as does Fourier-Bessel. If a feed is not located at the focal point of a parabolic reflector, we can see in Figs. 8.10 and 8.11 that the convergence behaviors of both methods are slowed. Even if the value of P is increased, the accuracies drop in regions far from boresight, especially for the Fourier-Bessel algorithm.

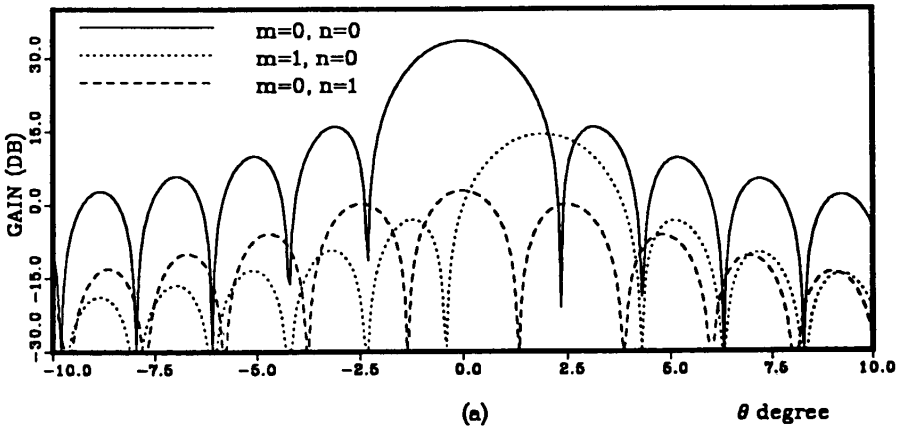

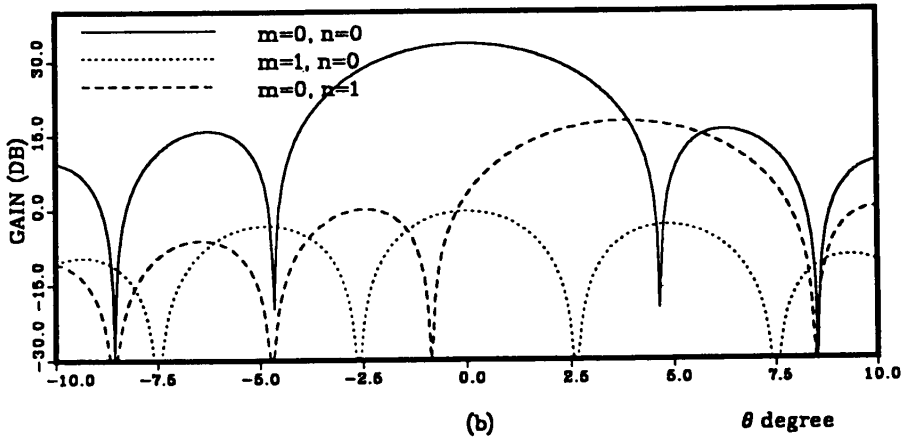

Figure 8.4 Contributions of three major series terms to the radiated far-field pattern, $a = 15\lambda$, $a/b = 2.0$, $F = 30\lambda$, $H = 18\lambda$, $q_1 = 7.14$, $q_2 = 44.9$, $t = (-18\lambda, 0, 0)$, $P, M, N = (1, 16, 8)$ for Fourier-Bessel algorithm; (a) $\phi = 0°$, (b) $\phi = 90°$.

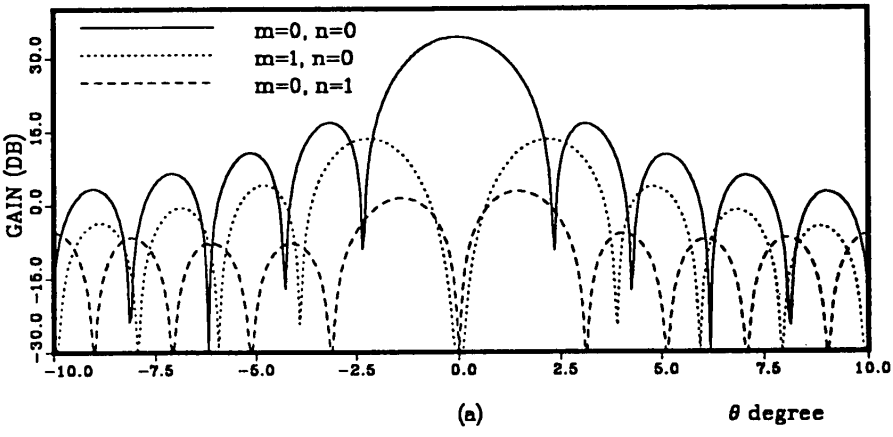

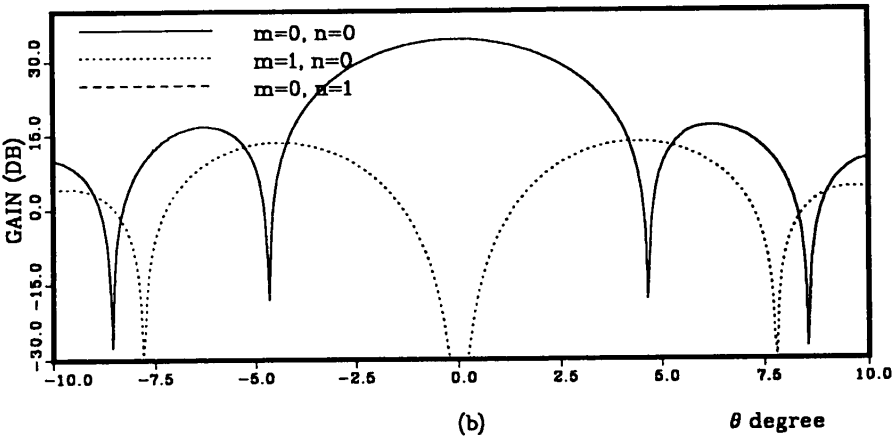

Figure 8.5 Contributions of three major series terms to the radiated far-field pattern, $a = 15\lambda$, $a/b = 2.0$, $F = 30\lambda$, $H = 18\lambda$, $q_1 = 7.14$, $q_2 = 44.9$, $t = (-18\lambda, 0, 0)$, $P, M, N = (1, 7, 7)$ for Jacobi-Bessel algorithm; (a) $\phi = 0°$, (b) $\phi = 90°$.

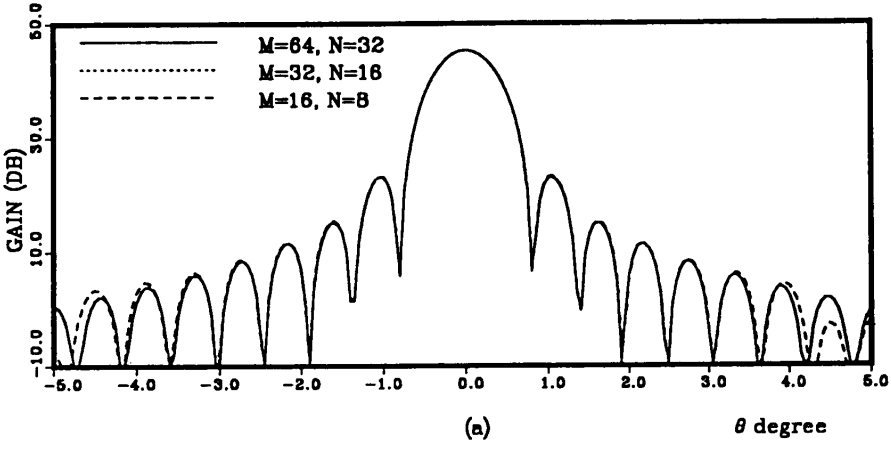

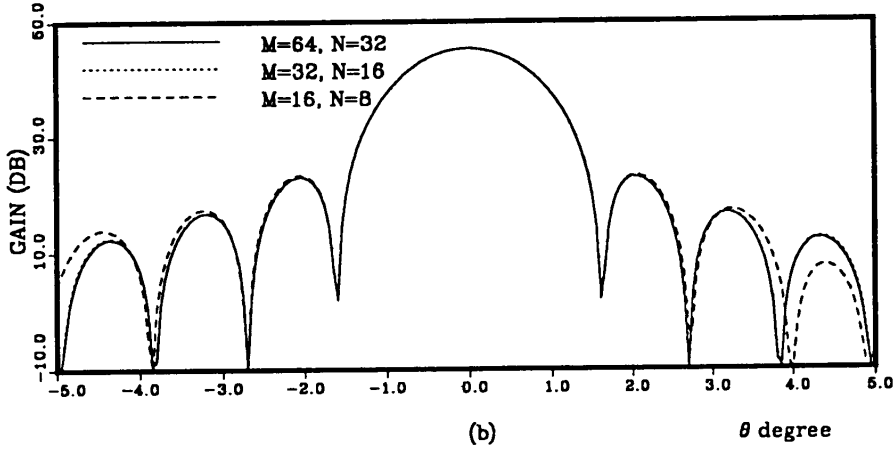

Figure 8.6 Convergence behavior of Fourier-Bessel Technique for a large and low eccentricity elliptical aperture, $a = 50\lambda, a/b = 2.0, F = 240\lambda, H = 70\lambda$, $q_1 = 54.80, q_2 = 220.79, t = (-70\lambda, 0, 0), P = 2$; **(a)** $\phi = 0°$, **(b)** $\phi = 90°$.

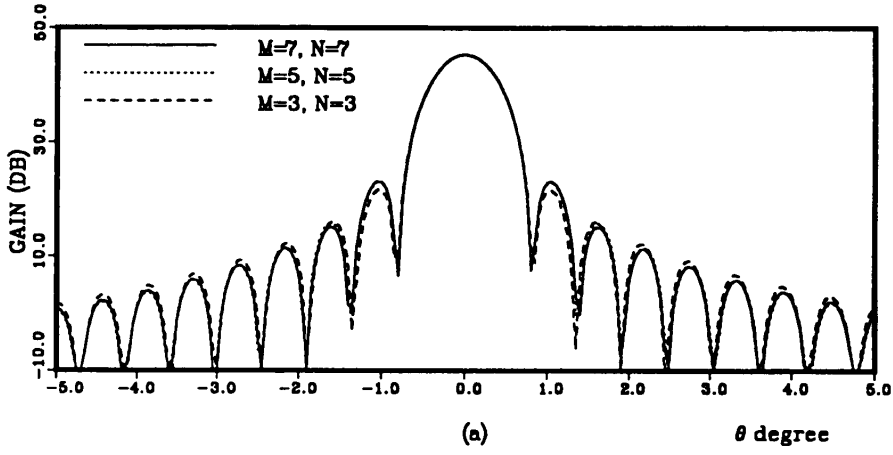

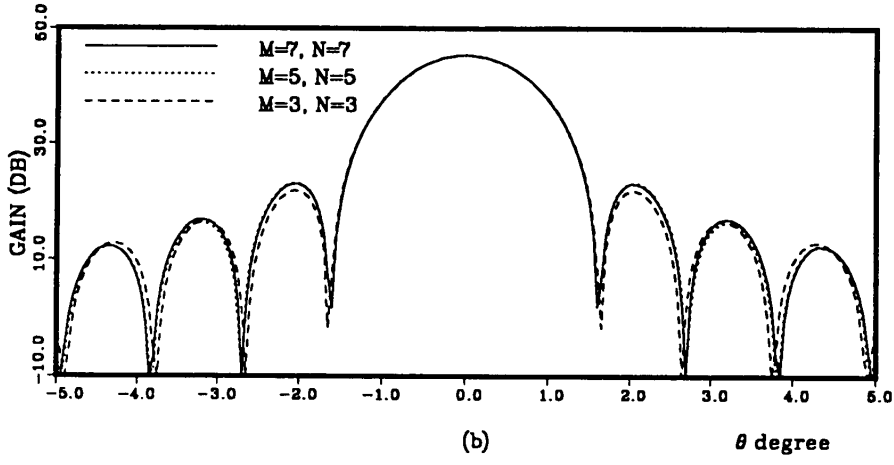

Figure 8.7 Convergence behavior of Jacobi-Bessel Technique for a large and low eccentricity elliptical aperture, $a = 50\lambda$, $a/b = 2.0$, $F = 240\lambda$, $H = 70\lambda$, $q_1 = 54.80$, $q_2 = 220.79$, $t = (-70\lambda, 0, 0)$, $P = 2$; (a) $\phi = 0°$, (b) $\phi = 90°$.

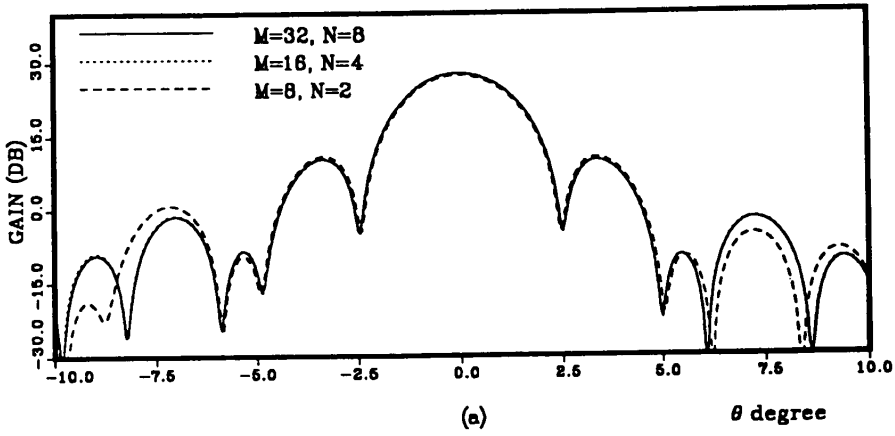

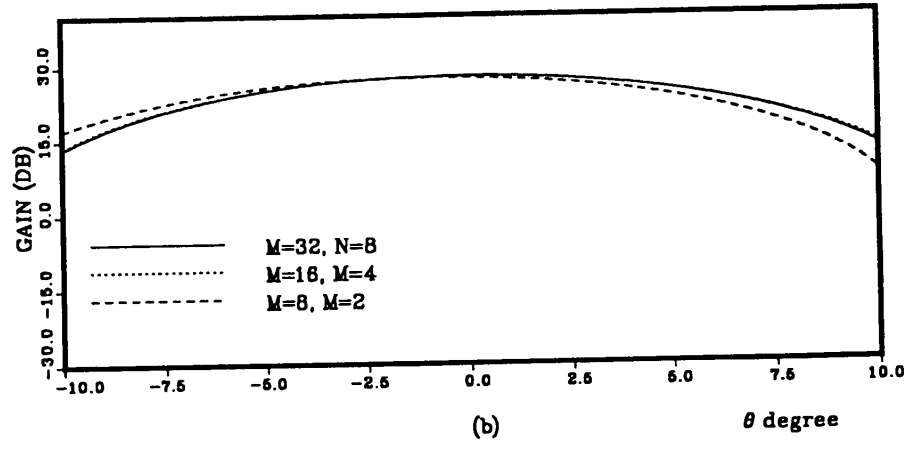

Figure 8.8 Convergence behavior of Fourier-Bessel Technique for a high eccentricity elliptical aperture, $a = 15\lambda$, $a/b = 5.0$, $F = 30\lambda$, $H = 18\lambda$, $q_1 = 7.14$, $q_2 = 274.72$, $t = (-18\lambda, 0, 0)$, $P = 2$; (a) $\phi = 0°$, (b) $\phi = 90°$.

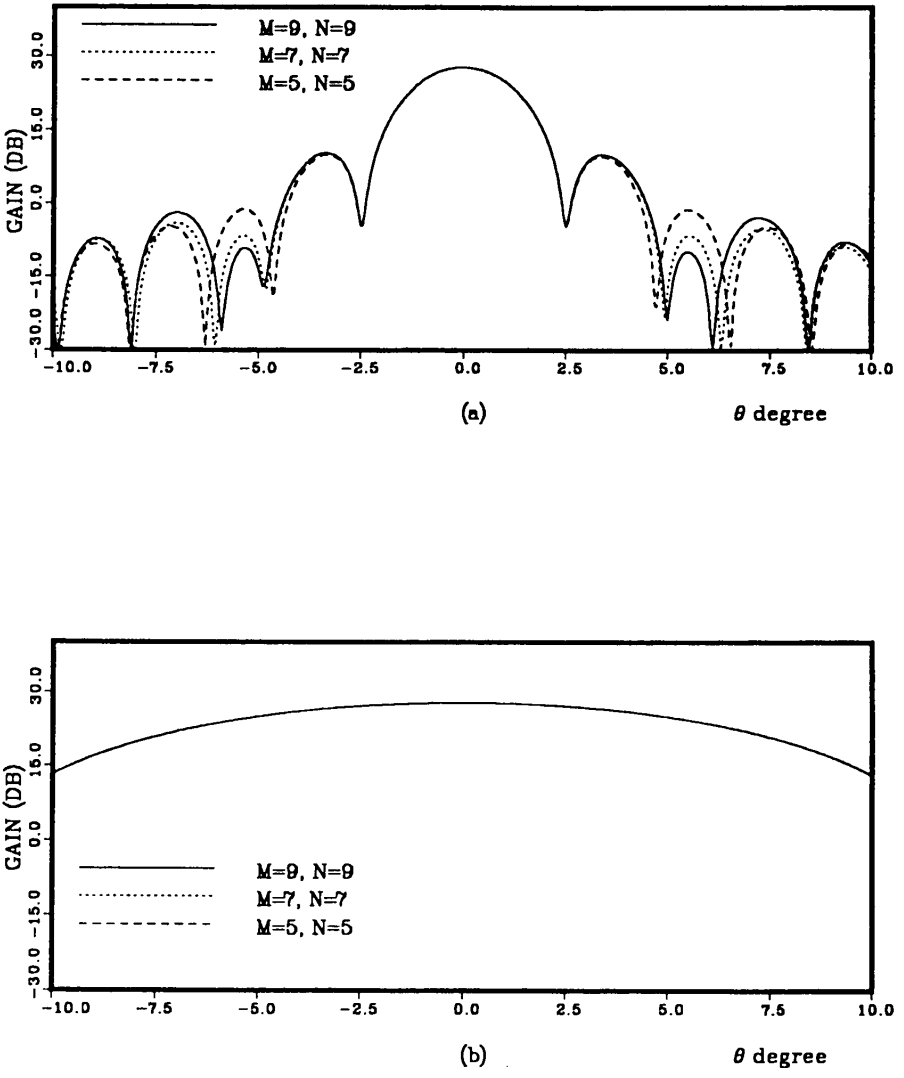

Figure 8.9 Convergence behavior of Jacobi-Bessel Technique for a high eccentricity elliptical aperture, $a = 15\lambda$, $a/b = 5.0$, $F = 30\lambda$, $H = 18\lambda$, $q_1 = 7.14$, $q_2 = 274.72$, $t = (-18\lambda, 0, 0)$, $P = 2$; **(a)** $\phi = 0°$, **(b)** $\phi = 90°$.

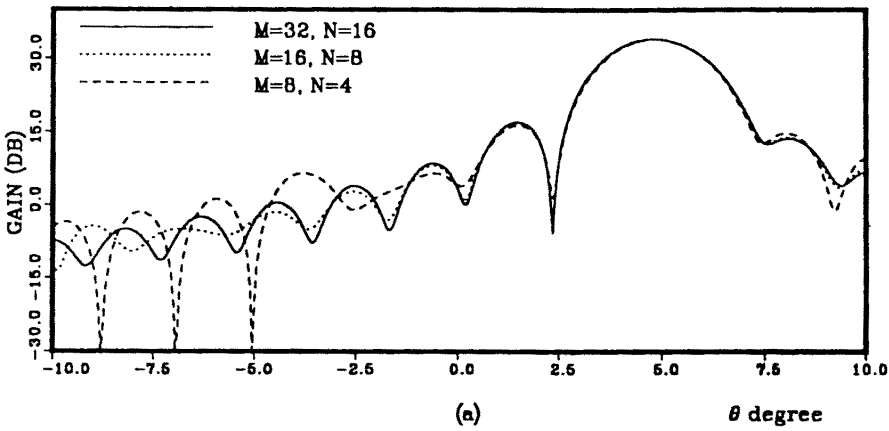

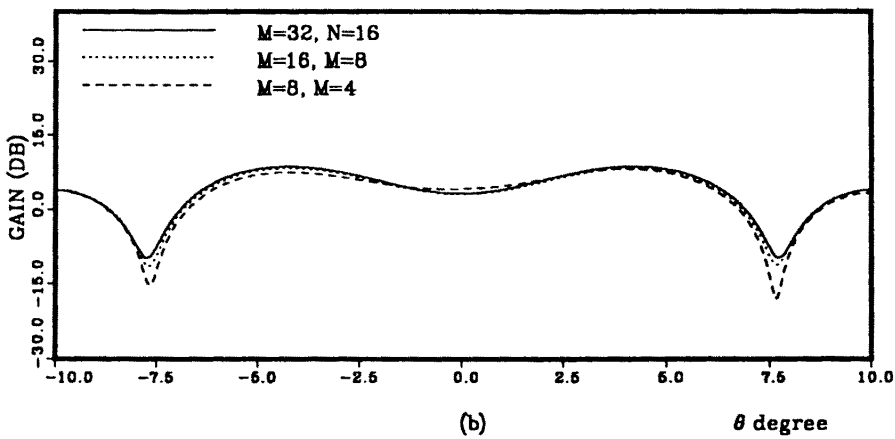

Figure 8.10 Convergence behavior of Fourier-Bessel Technique for a low eccentricity elliptical aperture when a feed is not located at focal point, $a = 15\lambda$, $a/b = 2.0$, $F = 30\lambda$, $H = 18\lambda$, $q_1 = 7.14$, $q_2 = 44.9$, $t = (-20\lambda, 0, -2\lambda)$, $P = 3$; (a) $\phi = 0°$, (b) $\phi = 90°$. Note that the beam peak is at $\theta = 4.8°$ in $\phi = 0°$ plane and, therefore, the pattern shown in (b) does not pass through the peak.

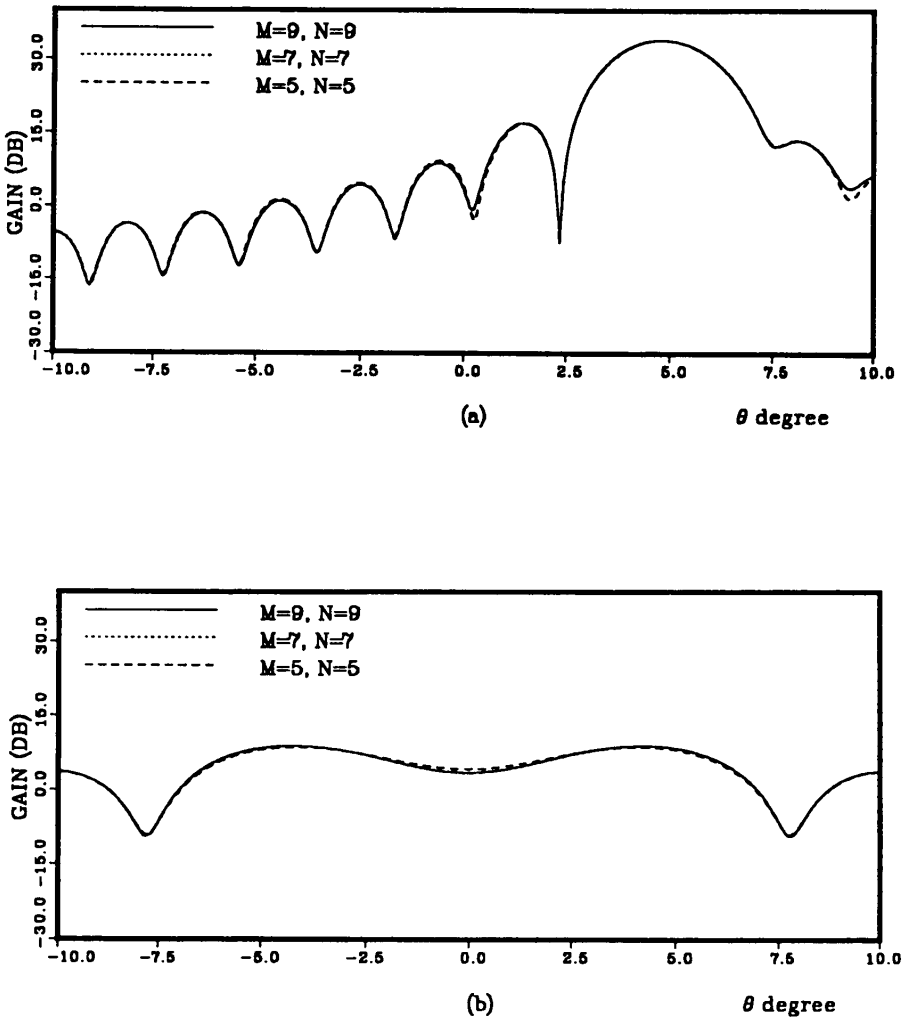

Figure 8.11 Convergence behavior of Jacobi-Bessel Technique for a low eccentricity elliptical aperture when a feed is not located at focal point, $a = 15\lambda$, $a/b = 2.0$, $F = 30\lambda$, $H = 18\lambda$, $q_1 = 7.14$, $q_2 = 44.9$, $t = (-20\lambda, 0, -2\lambda)$, $P = 3$; (a) $\phi = 0°$, (b) $\phi = 90°$. Note that the beam peak is at $\theta = 4.8°$ in $\phi = 0°$ plane and, therefore, the pattern shown in (b) does not pass through the peak.

Fourier-Bessel				Jacobi-Bessel			
Figure 6				Figure 7			
P=2	M=64	N=32	3.29 min	P=2	M=7	N=7	0.60 min
P=2	M=32	N=16	0.68 min	P=2	M=5	N=5	0.40 min
P=2	M=16	N=8	0.37 min	P=2	M=3	N=3	0.30 min
Figure 8				Figure 9			
P=2	M=32	N=8	0.66 min	P=2	M=9	N=9	1.20 min
P=2	M=16	N=4	0.30 min	P=2	M=7	N=7	0.86 min
P=2	M=8	N=2	0.18 min	P=2	M=5	N=5	0.46 min
Figure 10				Figure 11			
P=3	M=32	N=16	1.92 min	P=3	M=9	N=9	1.23 min
P=3	M=16	N=8	0.73 min	P=3	M=7	N=7	0.84 min
P=3	M=8	N=4	0.49 min	P=3	M=5	N=5	0.62 min

Table 8.1 Comparison of computing time between Fourier-Based and Jacobi-Bessel algorithms with an IBM 3090.

8.4 Conclusion

In this chapter, we have developed the Fourier-Bessel expansion method for reflector antennas with elliptical apertures. It is shown that the final result can be expressed in terms of Bessel functions only, even though, initially, the radiation integral is written in terms of Mathieu functions. The numerical convergence behaviors are discussed and compared with those of Jacobi-Bessel method. Each shows superior computational efficiency to the other for certain applications. For large and low eccentricity elliptical apertures, Jacobi-Bessel shows its superiority. Whereas, for very high eccentricity ellipses, Fourier-Bessel is much faster but is more sensitive to the location of a feed than Jacobi-Bessel.

The computer program of the Fourier-Bessel algorithm is quite similar to that of the Jacobi-Bessel method. Most of the subprograms are exactly identical. Thus, it is not difficult to write a program which can implement either algorithm. If this is done, one can harness the strength of each algorithm and can get accurate results very efficiently

for every type of reflector antenna with an elliptical aperture. Also, the techniques discussed in this chapter can be used for any elliptical-type aperture antennas.

Appendix A

For the elliptical projected aperture, the elliptical coordinate system is introduced and radial and angular Mathieu functions are used in the integral as expressed in (17). To evaluate (17), we have to use some of the properties of the radial and angular Mathieu functions which are well described in [9]. First, $Ce_i(\xi, q_{mn})$ and $Se_i(\xi, q_{mn})$ are solutions of the Mathieu differential equation, i.e.,

$$\frac{\partial^2 X}{\partial \xi^2} - (c - 2q_{mn}\cosh 2\xi)X = 0 \tag{30}$$

where c is the eigenvalue for a given q_{mn}. From (30), we obtain the following equation:

$$\int_0^{\xi_0} X \cosh 2\xi \, d\xi = \frac{c}{2q_{mn}} \int_0^{\xi_0} X \, d\xi - \frac{1}{2q_{mn}} \left[\frac{\partial X(\xi = \xi_0)}{\partial \xi} - \frac{\partial X(\xi = 0)}{\partial \xi} \right] \tag{31}$$

Similarly, since $ce_i(\xi, q_{mn})$ and $se_i(\xi, q_{mn})$ are solutions of

$$\frac{\partial^2 Y}{\partial \eta^2} + (c - 2q_{mn}\cos 2\eta)Y = 0 \tag{32}$$

the following equation is obtained.

$$\int_0^{\eta_0} Y \cos 2\eta \, d\eta = \frac{c}{2q_{mn}} \int_0^{\eta_0} Y \, d\eta + \frac{1}{2q_{mn}} \left[\frac{\partial Y(\eta = \eta_0)}{\partial \eta} - \frac{\partial Y(\eta = 0)}{\partial \eta} \right] \tag{33}$$

Finally, the angular Mathieu functions can be written as Fourier series i.e.,

$$ce_{2r}(\eta, q_{mn}) = \sum_{i=0}^{\infty} A_{2i}^{(2r)} \cos(2i)\eta \tag{34}$$

$$ce_{2r+1}(\eta, q_{mn}) = \sum_{i=0}^{\infty} A_{2i+1}^{(2r+1)} \cos(2i+1)\eta \tag{35}$$

$$se_{2r+1}(\eta, q_{mn}) = \sum_{i=0}^{\infty} B_{2i+1}^{(2r+1)} \sin(2i+1)\eta \tag{36}$$

$$se_{2r+2}(\eta, q_{mn}) = \sum_{i=0}^{\infty} B_{2i+2}^{(2r+2)} \sin(2i+2)\eta \tag{37}$$

where $A_i^{(r)}$ and $B_i^{(r)}$ are expansion coefficients of Mathieu functions.

The properties of Mathieu functions described before are used to produce the following useful equations:

$$\int_0^{2\pi} ce_{2r}(\eta, q_{mn})\, d\eta = 2\pi A_0^{(2r)} \tag{38}$$

$$\int_0^{2\pi} ce_{2r}(\eta, q_{mn}) \cos 2\eta\, d\eta = \frac{c\pi}{q_{mn}} A_0^{(2r)} \tag{39}$$

and

$$\begin{aligned} \int_0^{2\pi} ce_{2r+1}(\eta, q_{mn})\, d\eta &= \int_0^{2\pi} se_{2r+1}(\eta, q_{mn})\, d\eta \\ &= \int_0^{2\pi} se_{2r+2}(\eta, q_{mn})\, d\eta = 0 \end{aligned} \tag{40}$$

$$\begin{aligned} \int_0^{2\pi} ce_{2r+1}(\eta, q_{mn}) \cos 2\eta\, d\eta &= \int_0^{2\pi} se_{2r+1}(\eta, q_{mn}) \cos 2\eta\, d\eta \\ &= \int_0^{2\pi} se_{2r+2}(\eta, q_{mn}) \cos 2\eta\, d\eta \\ &= \text{ρ} \end{aligned} \tag{41}$$

Also

$$\begin{aligned} \int_0^{\xi_0} Ce_{2r}(\xi, q_{mn}) \cosh 2\xi\, d\xi = &\frac{c}{2q_{mn}} \int_0^{\xi_0} Ce_{2r}(\xi, q_{mn})\, d\xi \\ &- \frac{1}{2q_{mn}} Ce\prime_{2r}(\xi_0, q_{mn}) \end{aligned} \tag{42}$$

If (38) through (42) are substituted into (17), we get (19).

References

[1] Rahmat-Samii, Y., R. Mittra, and V. Galindo-Israel, "Computation of Fresnel and Fraunhofer fields of planar apertures and reflector antennas by Jacobi-Bessel series – A review," *Electromagn.*, **1**, 155–185, April–June 1981.

[2] Rahmat-Samii, Y., and V. Galindo-Israel, "Shaped reflector antenna analysis using the Jacobi-Bessel series," *IEEE Trans. Antennas Propagat.*, **AP-28**, 425–435, July 1980.

[3] Mittra, R., W. E. Ko, and M. S. Sheshadri, "A transform technique for computing the radiation pattern of prime-focal and cassegrainian reflector antennas," *IEEE Trans. Antennas Propagat.*, **AP-30**, 520–524, May 1982.

[4] Hung, C. S., and R. Mittra, "Secondary pattern and focal region distribution of reflector antennas under wide-angle scanning," *IEEE Trans. Antennas Propagat.*, **AP-31**, 99–103, Sept. 1983.

[5] Rahmat-Samii, Y., "Jacobi-Bessel analysis of reflector antennas with elliptical apertures," *IEEE Trans. Antennas Propagat.*, **AP-35**, 1070–1073, Sept. 1987.

[6] Wang, J. Y., and D. E. Silva, "Wave-front interpretation with Zernike polynomials," *Applied Optics*, **19**, 1510–1518, May 1980.

[7] Cornbleet, S., *Microwave Optics*, New York, Academic Press, 1976.

[8] Lam, P. T., S. W. Lee, C. C. Hung, and R. Acosta, "Strategy for reflector pattern calculation: Let the computer do the work," *IEEE Trans. Antennas Propagat.*, **AP-34**, 592–595, April 1986.

[9] Kim, C. S., "Scattering of an obliquely incident wave by a multilayered elliptical lossy cylinder," *Ph.D. Dissertation*, UCLA, Los Angeles, June 1989.

[10] McLachlan, N. W., *Theory and Application of Mathieu Function*, London, Oxford University Press, 1947.

[11] Rahmat-Samii, Y., "Reflector Antennas" in Y. Lo and S. Lee eds., *Antenna Handbook*, New York, Van Nostrand Reinhold Co., 1988.